Biomolecular condensates undergo a generic shear-mediated liquid-to-solid transition

Yi Shen[1], Francesco Simone Ruggeri[1], Daniele Vigolo[2], Ayaka Kamada[1], Seema Qamar[3], Aviad Levin[1], Christiane Iserman[4], Simon Alberti[4], Peter St George-Hyslop[3,5], Tuomas P. J. Knowles[1,6]*

1. Centre for Misfolding Diseases, Department of Chemistry, University of Cambridge, CB2 1EW Cambridge, UK
2. School of Chemical Engineering, University of Birmingham, B15 2TT Birmingham, UK
3. Cambridge Institute for Medical Research, Department of Clinical Neurosciences, University of Cambridge, CB2 0XY Cambridge, UK
4. Max Planck Institute of Molecular Cell Biology and Genetics, 01307 Dresden, Germany
5. Department of Medicine, Division of Neurology, University of Toronto and University Health Network, ON M5T 0S8 Toronto, Canada
6. Cavendish Laboratory, University of Cambridge, CB3 0HE Cambridge, UK

* e-mail: tpjk2@cam.ac.uk;

Membraneless organelles resulting from liquid-liquid phase separation of proteins control essential cellular functions, including mRNA processing, cytoplasm structuring, cell signalling and embryogenesis[1–4]. It has recently been discovered that the RNA-binding protein Fused in Sarcoma (FUS) can undergo a further irreversible phase transition, forming solid nanoscale aggregates, that associated with neurodegenerative disease[5–7]. While the irreversible gelation of protein condensates is generally related to malfunction and disease, one case where the liquid-to-solid transition (LST) of protein condensates is functional, however, is that of silk spinning[8,9]. The formation of silk fibrils is largely driven by shear, yet it is not known what factors control the pathological gelation of functional condensates. Here we demonstrate that four proteins and one peptide system with no function associated with fibre formation, have a strong propensity to undergo LST when exposed to even low levels of mechanical shear, once present in their liquid-liquid phase separated form. Using microfluidics to control the application of shear, we generated fibres from single protein condensates and characterized their structural and material properties as a function of shear stress. Our results reveal generic backbone-backbone hydrogen bonding constraints as a determining factor in governing this transition. These observations suggest that shear plays an important role in the irreversible LST of protein condensates, shed light on the role of physical factors in driving this transition in protein aggregation related diseases, and open a new route towards artificial shear responsive biomaterials.

Liquid-liquid phase separation (LLPS) underlies the spontaneous decomposition of a homogeneous solution into solute-rich and solute poor-phases, and has been studied in coacervation processes[10] in colloidal and polymer systems. Recently it has been discovered that LLPS occurs inside living cells and is a crucial process in the spatial organisation of the cytoplasm and nucleus[2]. LLPS also occurs for synthetic co-polymers[11] and extracellular proteins[8], including ones used in natural structural materials. In particular, during silk spinning, the precursor protein molecules are stored in liquid-liquid phase separated form. Crucially, liquid-liquid phase separated silk undergoes a liquid-to-solid transition (LST) to generate fibres mediated by mechanical shear[8,12–14]. It is increasingly recognised, however, that a wide range of other proteins present as functional condensates[15,16] can also undergo a LST process to form pathological solid protein aggregates which are associated with a wide range of diseases[5]. Yet, whether such functional protein condensates can also undergo an LST driven by mechanical shear remains unexplored.

In order to explore the generality of the shear mediated LST from protein condensates, we selected a representative set of systems, including the RNA-binding proteins FUS and Ded1 from human and yeast cells, respectively, human membrane-binding protein Annexin A11, carboxybenzyl protected diphenylalanine (zFF) peptide[17] and reconstituted silk protein. The monomeric solution of FUS protein is stable at high salt concentrations but undergoes LLPS when the salt concentration is lowered to the physiological range[5]. By using a pair of tweezers to generate mechanical deformation and induce shear forces, immediately following LLPS, we were able to pull solid fibres of 5-10 μm in diameter and 0.5-1 cm in length out from the droplet-containing solution (Fig. 1). Next, using a similar approach, we induced phase separation in a solution of Ded 1 protein by lowering the pH from 7.2 to 6.0 in PIPES buffer, whereas A11, zFF and silk protein were induced to undergo LLPS through addition of an aqueous solution of 10 % dextran. Within 5 min after the LLPS was induced, while droplets were still fusing and in their liquid state [5,6,17,18] (Movie S1-5), we were able to pull solid fibres from the condensates of all of these proteins and peptides by applying mechanical force (Fig. 1a). Notably, FUS, Ded1, A11 and zFF, a short peptide composed of only two amino acids, exhibited shear induced fibre formation from liquid condensates similar to that of the silk protein[8,9], although they have no shared primary structure beyond possessing intrinsically disordered, low complexity domains,

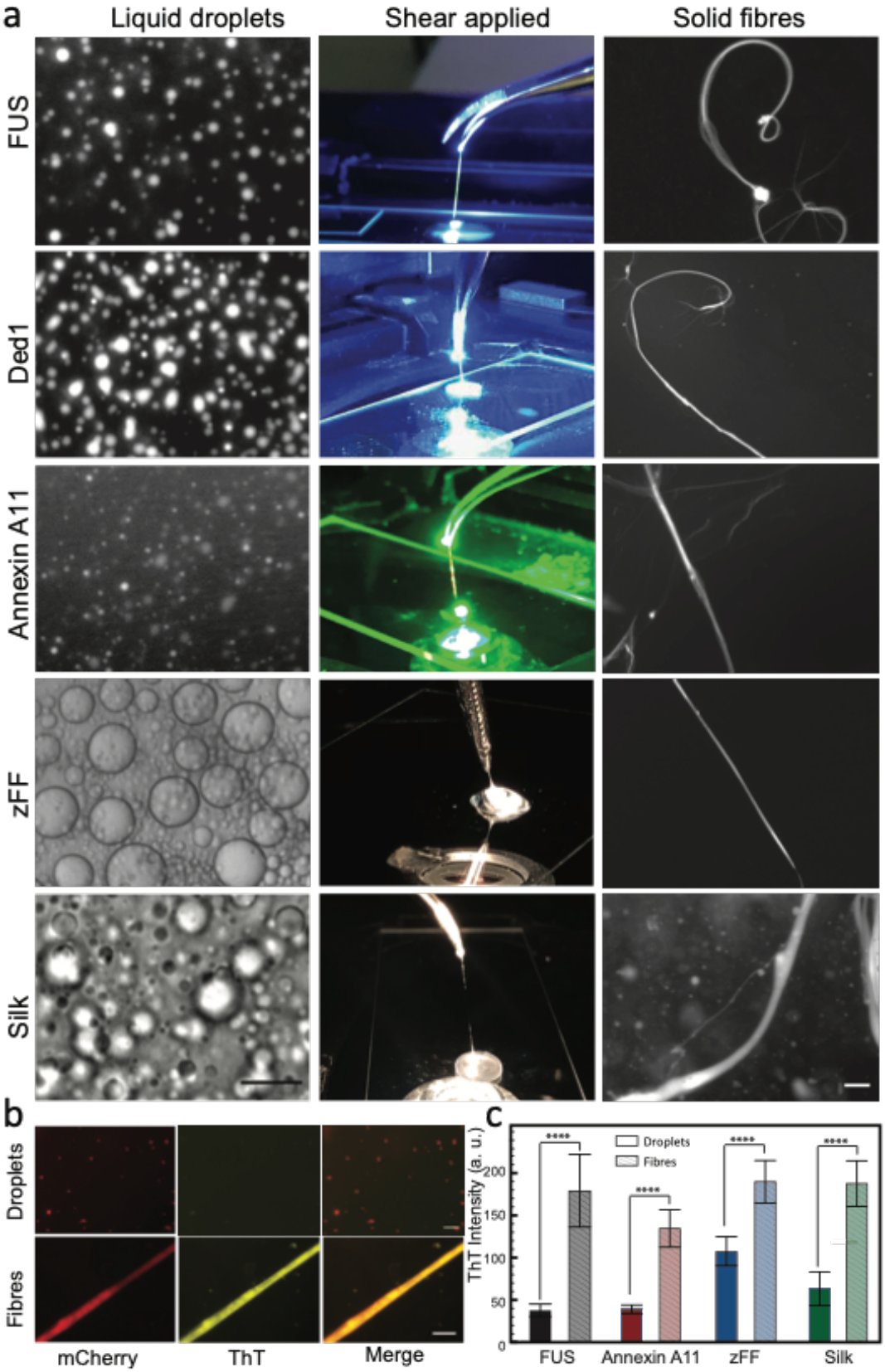

Figure 1: Fibre formation from liquid-liquid phase separated proteins and peptides is observed generically as a result of shear. a. LLPS of FUS (GFP), Ded1 (GFP), Annexin A11 (mCherry), zFF and silk was induced by lowering the salt concentration, lowering the pH value and mixing with 10% dextran respectively (left column). Shear was applied by pulling the solution with a pair of tweezers

(middle column). Fibre formation was observed by fluorescence microscopy (right column). zFF and silk fibre were stained with ThT. The scale bars of the first and third row of images are 20 µm. **b**. ThT staining of mCherry-tagged FUS droplets (top) and a fibre (bottom). Scale bars are both 5 µm. **c**. Fluorescence intensity of droplets and fibres after ThT staining for mCherry-tagged FUS (black), Annexin A11 (red), zFF (blue) and silk (green). Error bars show one standard deviation. A two-tailed T-test is applied for the statistical analysis. Since GFP emission wavelengths overlap with ThT staining, data for Ded1-GFP is not shown.

We further studied the change in the secondary structure of the protein condensates prior to and following the application of shear. We first monitored qualitatively the structural changes of the droplets by staining mCherry-tagged FUS, Annexin A11 and unlabelled zFF and silk protein with Thioflavin T (ThT), which binds specifically to β-sheet rich structures. The FUS fibres obtained as a result, exhibited significantly stronger ThT signal compared to that of liquid droplets immediately following LLPS (Fig. 1b), suggesting a structural transition from a disordered to a β-sheet rich ordered structure. The other proteins and peptide exhibited a similar behaviour and the difference in ThT intensity of droplets and fibres is quantified and summarized in figure 1c. Next, we performed Fourier Transform Infrared spectroscopy (FTIR) measurements and analysis on bulk samples before and after the application of shear to further investigate the change in protein structure. Following shearing of the bulk solution, we observed a significant shift of the Amide band I to lower wavenumbers for FUS, Ded1 and silk protein, suggesting the formation of hydrogen bonding and structural rearrangement (Fig. S2). However, due to the heterogeneity of the bulk samples, the change was not significant for Annexin A11 and zFF.

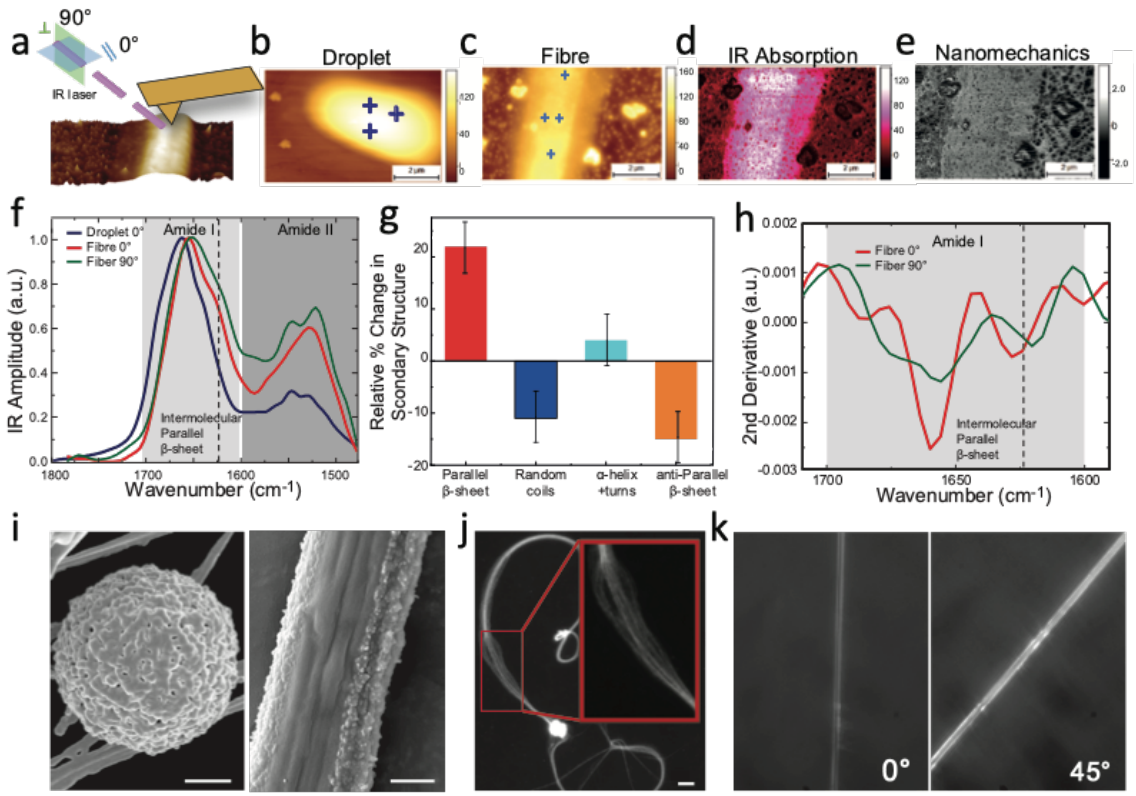

Figure 2: Structural changes in FUS protein droplets following application of mechanical shear. **a.** Scheme of the measurement setup for polarized infrared nanospectroscopy (AFM-IR) on a single fibre with polarized light source parallel (0°) and perpendicular (90°) to the deposition surface. 3D morphology map of a droplet (**b.**) and fibre (**c.**) Crosses indicate the locations of the spectroscopy

measurements. **d.** Map of IR absorption in the Amide I band (1655 cm^{-1}). **e.** Map of the nanomechanical properties of the fibre[7]. **f**. Nanoscale localized IR spectrum as a function of the polarization angle of a droplet at 0° (blue line), fibre at 0°(red line) and 90° (green line). Spectra were acquired at the positions indicated by the blue crosses. **g.** Relative change in secondary structure between droplets and fibres (error bar ±SD) **h**. Second derivative of the IR spectrum of the fibre with polarization 0° (red line) and 90° (green line). **i.** Scanning electron microscopy (SEM) images of a droplet aged for 1 h and a fibre (scale bars 500 nm). **j**. Fluorescence microscopy image of a FUS fibre in 50 mM tris buffer. Aligned nanofibrils within the fibre are shown in the zoomed in insert. The scale bar is 20 μm. **k.** Polarization microscopy images of a fibre at 0° and 45°.

In order to exclude the influence of sample heterogeneity and further investigate the structural transitions occurring during fibre formation at a single droplet and single fibre resolution, we focused on the FUS protein system and exploited the capabilities of polarized infrared nanospectroscopy (AFM-IR) (Fig. 2a). By using AFM-IR, we acquired 3D morphology, IR absorption and stiffness maps of the FUS samples with nanoscale resolution[7,19,20]. We first acquired a morphology map of a single droplet (Fig. 2b). We then measured the morphology (Fig. 2c), IR absorption in the Amide I band at 1655 cm^{-1} (Fig. 2d) and nanomechanics (Fig. 2e) of a single fibre generated through application of mechanical shear. In particular, the IR and nanomechanical maps indicated that the formed fibres have spatially uniform biophysical properties. The Amide band I and II of the fibre are shifted toward lower wavenumbers than in the droplet, indicating the formation of intermolecular hydrogen bonding (Fig. 2f). Moreover, the appearance of a shoulder in the Amide I band at 1625 cm^{-1} indicates the formation of intermolecular β-sheets, in good agreement with the FTIR results from the bulk samples (Fig. S2a). The relative change in the secondary structure of droplets and fibres is presented in figure 2g. These results present the relative increase in formation of parallel β-sheet and α-helix content, and a reduction in antiparallel β-sheet and random coil in the fibres.

To obtain further structural characterisation of the fibrillar state, we compared the AFM-IR spectra acquired with polarized light source parallel (0°) and perpendicular (90°) to the deposition surface. The IR spectrum of the fibre changed as a function of the polarization. In particular, at an angle of 90°, a stronger shift toward lower wavenumbers of the Amide band I and a more pronounced shoulder at 1625 cm^{-1} were detected (Fig. 2f).(Fig. 2h). This polarization effect demonstrates that the structure of the fibre is anisotropically ordered and that there are more intermolecular β-sheets oriented perpendicular to the fibre axis[21].

We next performed scanning electron microscopy (SEM) to characterize the structural morphology of the FUS liquid droplet and fibrillar phases. The micrographs revealed a porous network for FUS droplets and elongated rod-shaped fibres with aligned nanofibrils (Fig. 2i). The alignment of the nanofibrils within the fibre was also observed through fluorescence microscopy (Fig. 2j). This anisotropy was further confirmed by polarization microscopy, which showed a maximum birefringence signal at 45° (Fig. 2k), indicating that the fibres contain highly aligned nanofibrils. Taken together, these results highlight the key role of backbone-backbone hydrogen bonding in driving the LTS.

In order to test this idea, we next focused on PR repeat peptides which possess the ability to undergo LLPS but due to the proline rich nature of the sequence, does not have a strong propensity for forming backbone-backbone hydrogen bonds[22]. Interestingly, our results (Fig. S3) show that this system is not able to undergo a LST as a result of application of shear unlike the other systems studied here, highlighting the significance of backbone-backbone hydrogen bonding in driving this transition.

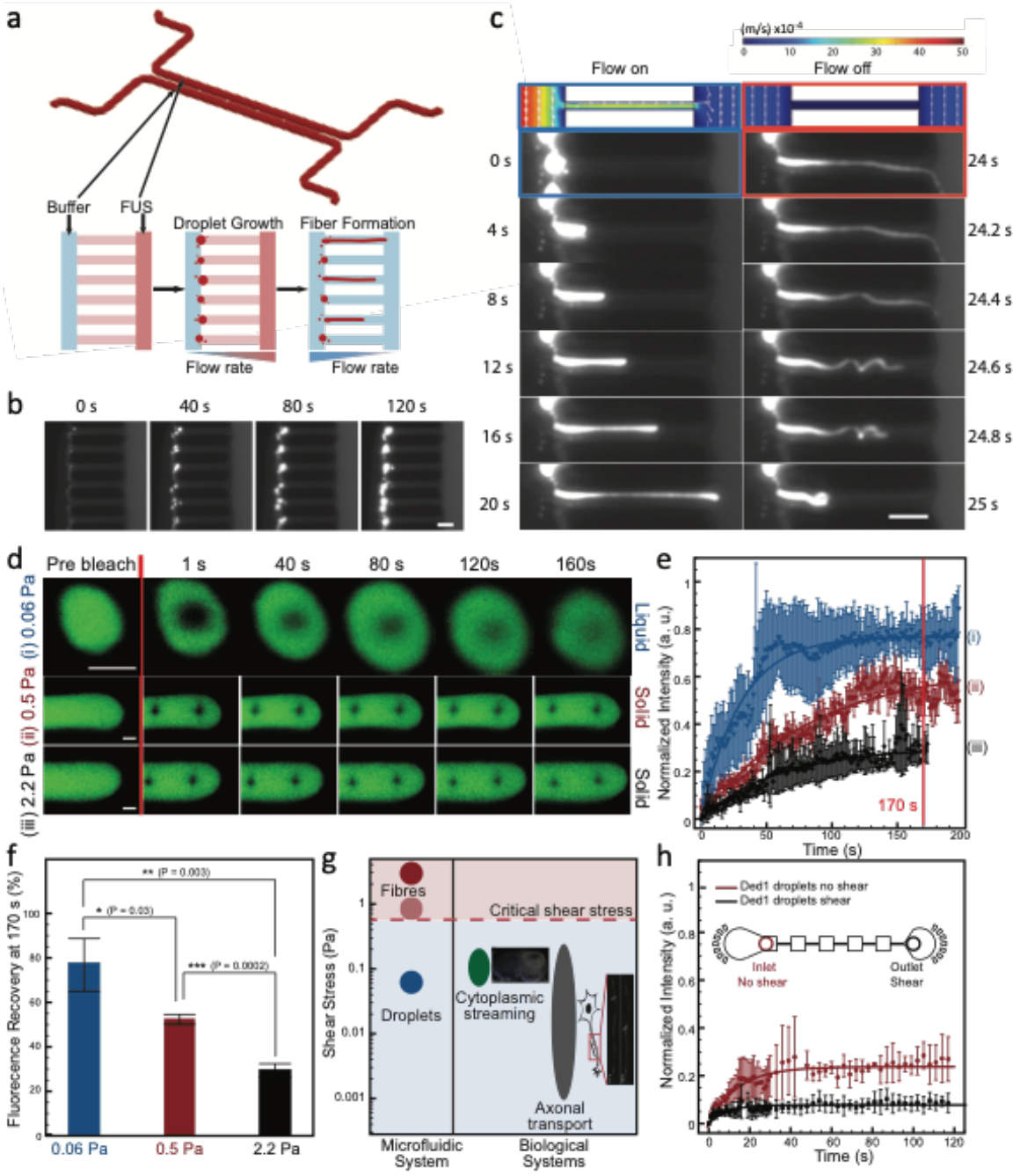

Figure 3. Shear mediated fibre formation probed by microfluidics. **a.** Microfluidic device design and schematic of droplets' growth and fibre formation under varied flow conditions. Two large flow chambers (with width × height, 50 × 25 µm) were connected with 5 series of small bridges (with 3 × 4.2, 5 × 4.2, 7 × 4.2, 9 × 4.2, 11 × 4.2 µm width × height) **b.** Time dependant fluorescence images of FUS droplets formation at the entrance of the small bridge channels, scale bar 5 µm. **c.** A single fibre was formed from a single droplet under shear with the flow on, which then retracted and curled when the applied pressure was turned off (Movie S6), scale bar 5 µm. 3D numerical simulation of the flow field when the shear was applied (top row). FRAP analysis: **d.** Image sequence (the scale bars are 1 µm**)** **e.** Curves, error bar ±SD and **f.** Average fluorescence recovery at 170 s of FUS droplets and fibres formed at different shear stress: (i) 0.06 Pa, (ii) 0.5 Pa and (iii) 2.2 Pa, n≥3, error bar ±SD, two-tailed T-test is applied for the statistical analysis. **g**. Comparison of the shear stress present in biological

systems: cytoplasmic streaming[2,26,27] and axonal transport[18,30–32] relative to the regime explored in this study. **h.** Ded1 droplets fluorescence recovery after bleaching before and after having experienced the shear in the constricted microfluidic channel, n≥3 error bar ±SD. The solid lines in e and h were drawn as a guide to the eye.

The effect of mechanical forces in such sol-gel transitions has been previously studied in polymer and colloidal systems[23,24]. In order to explore this phenomenon for liquid-liquid phase separated proteins in a quantitative manner, a microfluidic platform was developed to induce phase separation, apply controlled levels of shear stress and characterize the mechanical properties of the formed structures without drying taking place. Through this approach, we were first able to induce and control the phase separation within the channel. The design of the microfluidic device used is illustrated in Figure 3a. Two large flow chambers were connected by a series of small bridge channels (Fig. 3a). By modulating the flow rates in the two large chambers, different pressure drops have been obtained across the small bridges to generate variable levels of shear. We first induced phase separation by flowing FUS protein in the right chamber and low ionic strength buffer in the left chamber. The flow rates were chosen to generate a pressure gradient from the right to the left chamber to drive the protein solution through the bridging channels and allow phase separation at the entrance of the bridge channels (Fig. 3b). Time lapse microscopy of the process revealed the nucleation and subsequent growth of FUS droplets. Within 2 min, the droplets grew to i.e. 3 µm in diameter (Fig. 3b). We then rapidly applied a higher flow rate in the left chamber to increase the level of shear. By increasing the average shear stress from 0.06 to 0.5 Pa across the small bridges, liquid protein condensates can be seen to deform and elongate along the span of the bridge channel (Fig. 3c left). The pressure difference was then removed by applying the same flow rates in both chambers. Following this, the formed fibre was first seen to retract and then recoil back inside the bridge, indicating the formation of an elastic fibre from an initially liquid FUS protein droplet (Fig. 3c right). When we applied a lower shear stress of 0.22 Pa, the droplets remained spherical and did not form fibres. The experiments, together with 3D finite elements simulations (Fig 3c top) revealed a critical shear stress of 0.5 Pa which was found to trigger the fibre formation from the droplets. Detailed flow fields with varied flow rates at each shear stress and shear rate are summarized in Fig. S4 and Table S1.

We further characterized the dynamics of the droplets and fibres by Fluorescence Recovery After Photobleaching (FRAP) measurements[25]. We found that the FUS droplets remain liquids as the fluorescence recovery reached up to ~75% after 170s when a shear stress below 0.06 Pa was applied. Once these droplets were deformed into solid fibres, however, by applying the critical shear stress of 0.5 Pa, only ~52% of the fluorescence was found to be recovered after 170 s. Finally, by applying an even higher shear stress of 2.2 Pa, the formed fibres only recovered ~27% of their initial fluorescence intensity after 170 s (Fig. 3d–f).

It is interesting to note that these shear stress values are comparable to those reported in biologically relevant systems. In fact, the maximum shear stress that can be generated during cytoplasmic streaming ranges from 0.06 Pa (in *C. elegance* embryo cells)[2,26] to 0.2 Pa (in *Chara* cells)[27]. In human neuronal cells, slow axonal transport which has a “stop and go” motion pattern can generate shear stresses of c.a. 0.001 Pa with average transport rates and can reach c.a. 0.05 Pa at peak transport rates[28,29]. Moreover, fast axonal transport of vesicles and lysosomes, co-traffic with FUS-containing stress granules along the microtubes[18], can experience shear stress of c.a. 0.18 Pa even with at average transport rates[18,30–32] (see supplementary information) (Fig. 3g). Interestingly, these values are within the range tested here, and in particular the high end values are of the same order as magnitude of the critical shear value that the present work has revealed is able to trigger the LST, highlighting the danger of irreversible phase transition associated with cellular malfunction mediated by physical driving forces. We next tested Ded

1 condensates under shear by flowing the droplets directly through a channel with series of expansions and constrictions right after LLPS (Fig. 3h). The condensates at the inlet of the channel not exposed to shear had higher fluorescence recovery after bleaching (~22%) after 118 s than the ones at the outlet that had been exposed to shear (~7%) (Fig. 3h), showing a similar shear response as FUS protein. The general lower fluorescence recovery might be due to the wetting property of the Ded1 droplets on the glass surface, as shown in Movie S2.

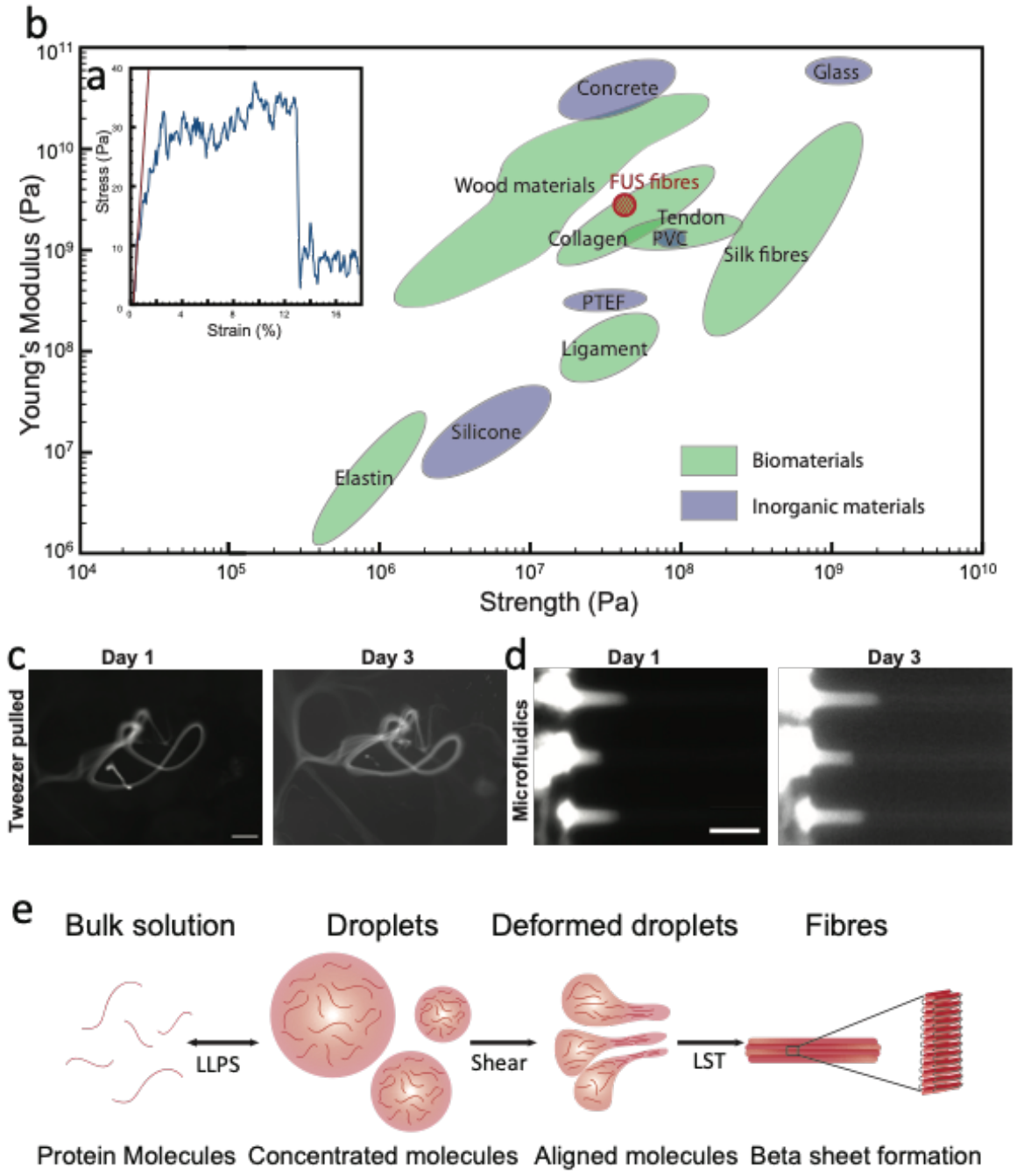

Figure 4: Material properties of fibres and proposed model of fibre formation from protein condensates under shear. a. Tensile strength measurement of a dried FUS fibre compared to other biomaterials in their dry states. **b.** Young's modulus versus strength of the FUS fibre compared to a range of biological and inorganic materials. The fibres formed by tweezer-pulling (**c**), scale bar, 100 µm, and microfluidics (**d**), scale bar, 10 µm, remained stable after 3 days incubation in the tris buffer

without shear. **e.** Protein molecules are concentrated in the droplets following LLPS. Shear aligns the molecules/oligomers inside the droplets and promotes inter-molecular interactions resulting in the formation of β-sheet rich fibres.

We estimated the Young's modulus of the wet FUS fibres directly after their formation in the microfluidic channel from the elastic response to pressure modulations (see supporting materials). The resulted value of c.a. 12 kPa is comparable to that found in many hydrogel systems[33,34], including silk fibroin hydrogels[35,36]. We next also characterized the mechanical properties dried FUS fibres by applying an increasing load until the point of fibre fracture (Fig. 4a). The results revealed a maximum tensile strength of 35 MPa, a toughness of 2.8 MJ/m^3 and a Young's modulus of approximately 3 GPa, which is comparable to dry silk fibres from cocoons[37,38] (Fig. 4b). This similarity can be rationalized by the fact that both fibrous materials are held together by a intermolecular β-sheet network.

To further investigate the thermodynamics of the phases connected by LST, we estimated the critical concentration of the soluble monomer phase in equilibrium with both the liquid and solid phases. We found that the critical monomer concentration in the samples containing fibres was significantly lower than the one in the sample containing only droplets (Fig. S5abc), indicating a higher level of thermodynamic stability of the fibrillar phase (see Methods section). Our results also show that the fibrillar morphology remained unchanged over several days, and that no conversion back to the liquid phase was observed (Fig. 4cd) in agreement with the higher thermodynamic stability of the solid phase. Crucially, therefore, under these conditions, the persistence of the liquid state is ensured by kinetic barriers that can be overcome by shear stress, which can help to align the protein molecules, promote inter-molecular interactions and trigger a phase transition that results in the formation of more thermodynamically stable fibres composed of aligned nanofibrils rich in intermolecular hydrogen bonded β-sheets (Fig. 4e).

In conclusion, we report a general shear response of peptides and proteins that can form solid fibres from phase separated liquid condensates. This process has striking similarities with that of silk fibre formation, yet is independent of the protein/peptide primary sequence. This phenomenon was probed with an array of microfluidic based approaches to allow for controlled LLPS and tuneable shear stress to be applied, inducing fibre formation from single droplets while minimizing the influence of any air-water interfaces. By capitalizing on this methodology, we were able to achieve shear conditions comparable to those found in cells. This observation suggests that nature has evolved mechanisms to protect against shear-mediated LST, and it is interesting to speculate that the heterogenous nature of many naturally occurring condensates can contribute to this protective effect as it decreases the effective concentration of each individual component in the liquid. More generally, our findings unveil the importance of mechanical shear for protein phase transitions that drive liquid condensates to form solid fibres, shedding light on the possible mechanisms involved in disease-related protein aggregation.

References

(1) Kedersha, N.; Stoecklin, G.; Ayodele, M.; Yacono, P.; Lykke-Andersen, J.; Fritzler, M. J.; Scheuner, D.; Kaufman, R. J.; Golan, D. E.; Anderson, P. Stress Granules and Processing Bodies Are Dynamically Linked Sites of MRNP Remodeling. *J. Cell Biol.* **2005**, *169*, 871–884.

(2) Brangwynne, C. P.; Eckmann, C. R.; Courson, D. S.; Rybarska, A.; Hoege, C.; Gharakhani, J.; Jülicher, F.; Hyman, A. A. Germline P Granules Are Liquid Droplets That Localize by Controlled Dissolution/Condensation. *Science* **2009**, *324*, 1729–1732.

(3) Wippich, F.; Bodenmiller, B.; Trajkovska, M. G.; Wanka, S.; Aebersold, R.; Pelkmans, L. Dual Specificity Kinase DYRK3 Couples Stress Granule Condensation/Dissolution to MTORC1

Signaling. *Cell* **2013**, *152*, 791–805.

(4) Strzelecka, M.; Trowitzsch, S.; Weber, G.; Lührmann, R.; Oates, A. C.; Neugebauer, K. M. Coilin-Dependent SnRNP Assembly Is Essential for Zebrafish Embryogenesis. *Nat. Struct. Mol. Biol.* **2010**, *17*, 403–409.

(5) Patel, A.; Lee, H. O.; Jawerth, L.; Maharana, S.; Jahnel, M.; Hein, M. Y.; Stoynov, S.; Mahamid, J.; Saha, S.; Franzmann, T. M.; *et al*. A Liquid-to-Solid Phase Transition of the ALS Protein FUS Accelerated by Disease Mutation. *Cell* **2015**, *162*, 1066–1077.

(6) Murakami, T.; Qamar, S.; Lin, J. Q.; Schierle, G. S. K.; Rees, E.; Miyashita, A.; Costa, A. R.; Dodd, R. B.; Chan, F. T. S.; Michel, C. H.; *et al*. ALS/FTD Mutation-Induced Phase Transition of FUS Liquid Droplets and Reversible Hydrogels into Irreversible Hydrogels Impairs RNP Granule Function. *Neuron* **2015**, *88*, 678–690.

(7) Qamar, S.; Wang, G.; Randle, S. J.; Ruggeri, F. S.; Varela, J. A.; Lin, J. Q.; Phillips, E. C.; Miyashita, A.; Williams, D.; Ströhl, F.; *et al*. FUS Phase Separation Is Modulated by a Molecular Chaperone and Methylation of Arginine Cation-π Interactions. *Cell* **2018**, *173*, 720-734.e15.

(8) Jin, H.-J.; Kaplan, D. L. Mechanism of Silk Processing in Insects and Spiders. *Nature* **2003**, *424*, 1057–1061.

(9) Heim, M.; Keerl, D.; Scheibel, T. Spider Silk: From Soluble Protein to Extraordinary Fiber. *Angew. Chemie Int. Ed.* **2009**, *48*, 3584–3596.

(10) de Kruif, C. G.; Weinbreck, F.; de Vries, R. Complex Coacervation of Proteins and Anionic Polysaccharides. *Curr. Opin. Colloid Interface Sci.* **2004**, *9*, 340–349.

(11) Ianiro, A.; Wu, H.; van Rijt, M. M. J.; Vena, M. P.; Keizer, A. D. A.; Esteves, A. C. C.; Tuinier, R.; Friedrich, H.; Sommerdijk, N. A. J. M.; Patterson, J. P. Liquid–Liquid Phase Separation during Amphiphilic Self-Assembly. *Nat. Chem.* **2019**, *11*, 320–328.

(12) Vollrath, F.; Porter, D.; Holland, C. The Science of Silks. *MRS Bull.* **2013**, *38*, 73–80.

(13) Holland, C.; Vollrath, F.; Ryan, A. J.; Mykhaylyk, O. O. Silk and Synthetic Polymers: Reconciling 100 Degrees of Separation. *Adv. Mater.* **2012**, *24*, 105–109.

(14) Vollrath, F.; Knight, D. P. Liquid Crystalline Spinning of Spider Silk. *Nature* **2001**, *410*, 541–548.

(15) Weber, S. C.; Brangwynne, C. P. Getting RNA and Protein in Phase. *Cell* **2012**, *149*, 1188–1191.

(16) Shin, Y.; Brangwynne, C. P. Liquid Phase Condensation in Cell Physiology and Disease. *Science* **2017**, *357*.

(17) Yuan, C.; Levin, A.; Chen, W.; Xing, R.; Zou, Q.; Herling, T. W.; Challa, P. K.; Knowles, T. P. J.; Yan, X. Nucleation and Growth of Amino Acid and Peptide Supramolecular Polymers through Liquid–Liquid Phase Separation. *Angew. Chemie* **2019**, *131*, 18284–18291.

(18) Liao, Y.-C.; Fernandopulle, M. S.; Wang, G.; Choi, H.; Hao, L.; Drerup, C. M.; Patel, R.; Qamar, S.; Nixon-Abell, J.; Shen, Y.; *et al*. RNA Granules Hitchhike on Lysosomes for Long-Distance Transport, Using Annexin A11 as a Molecular Tether. *Cell* **2019**, *179*, 147-164.e20.

(19) Ruggeri, F. S.; Longo, G.; Faggiano, S.; Lipiec, E.; Pastore, A.; Dietler, G. Infrared

Nanospectroscopy Characterization of Oligomeric and Fibrillar Aggregates during Amyloid Formation. *Nat. Commun.* **2015**, *6*, 1–9.

(20) Ruggeri, F.; Marcott, C.; Dinarelli, S.; Longo, G.; Girasole, M.; Dietler, G.; Knowles, T.; Ruggeri, F. S.; Marcott, C.; Dinarelli, S.; *et al*. Identification of Oxidative Stress in Red Blood Cells with Nanoscale Chemical Resolution by Infrared Nanospectroscopy. *Int. J. Mol. Sci.* **2018**, *19*, 2582.

(21) Ruggeri, F. S.; Byrne, C.; Khemtemourian, L.; Ducouret, G.; Dietler, G.; Jacquot, Y. Concentration-Dependent and Surface-Assisted Self-Assembly Properties of a Bioactive Estrogen Receptor α-Derived Peptide. *J. Pept. Sci.* **2015**, *21*, 95–104.

(22) Boeynaems, S.; Bogaert, E.; Kovacs, D.; Konijnenberg, A.; Timmerman, E.; Volkov, A.; Guharoy, M.; De Decker, M.; Jaspers, T.; Ryan, V. H.; *et al*. Phase Separation of C9orf72 Dipeptide Repeats Perturbs Stress Granule Dynamics. *Mol. Cell* **2017**, *65*, 1044-1055.e5.

(23) Ke, H.; Yang, L.-P.; Xie, M.; Chen, Z.; Yao, H.; Jiang, W. Shear-Induced Assembly of a Transient yet Highly Stretchable Hydrogel Based on Pseudopolyrotaxanes. *Nat. Chem.* **2019**, *11*, 470–477.

(24) Zebrowski, J.; Prasad, V.; Zhang, W.; Walker, L. .; Weitz, D. . Shake-Gels: Shear-Induced Gelation of Laponite–PEO Mixtures. *Colloids Surfaces A Physicochem. Eng. Asp.* **2003**, *213*, 189–197.

(25) Axelrod, D.; Koppel, D. E.; Schlessinger, J.; Elson, E.; Webb, W. W. Mobility Measurement by Analysis of Fluorescence Photobleaching Recovery Kinetics. *Biophys. J.* **1976**, *16*, 1055.

(26) Niwayama, R.; Nagao, H.; Kitajima, T. S.; Hufnagel, L.; Shinohara, K.; Higuchi, T.; Ishikawa, T.; Kimura, A. Bayesian Inference of Forces Causing Cytoplasmic Streaming in Caenorhabditis Elegans Embryos and Mouse Oocytes. *PLoS One* **2016**, *11*, e0159917.

(27) Goldstein, R. E.; van de Meent, J.-W. A Physical Perspective on Cytoplasmic Streaming. *Interface Focus* **2015**, *5*, 20150030.

(28) Brown, A. Axonal Transport of Membranous and Nonmembranous Cargoes: A Unified Perspective. *J. Cell Biol.* **2003**, *160*, 817–821.

(29) Brown, A. Slow Axonal Transport: Stop and Go Traffic in the Axon. *Nat. Rev. Mol. Cell Biol.* **2000**, *1*, 153–156.

(30) Kaether, C.; Skehel, P.; Dotti, C. G. Axonal Membrane Proteins Are Transported in Distinct Carriers: A Two-Color Video Microscopy Study in Cultured Hippocampal Neurons. *Mol. Biol. Cell* **2000**, *11*, 1213–1224.

(31) Ochs, S. Fast Axoplasmic Transport of Materials in Mammalian Nerve and Its Integrative Role. *Ann. N. Y. Acad. Sci.* **1972**, *193*, 43–58.

(32) Roy, S.; Zhang, B.; Lee, V. M.-Y.; Trojanowski, J. Q. Axonal Transport Defects: A Common Theme in Neurodegenerative Diseases. *Acta Neuropathol.* **2005**, *109*, 5–13.

(33) Li, X.; Chen, S.; Li, J.; Wang, X.; Zhang, J.; Kawazoe, N.; Chen, G. 3D Culture of Chondrocytes in Gelatin Hydrogels with Different Stiffness. *Polymers (Basel).* **2016**, *8*, 269.

(34) Vigolo, D.; Ramakrishna, S. N.; deMello, A. J. Facile Tuning of the Mechanical Properties of a

Biocompatible Soft Material. *Sci. Rep.* **2019**, *9*, 7125.

(35) Chao, P.-H. G.; Yodmuang, S.; Wang, X.; Sun, L.; Kaplan, D. L.; Vunjak-Novakovic, G. Silk Hydrogel for Cartilage Tissue Engineering. *J. Biomed. Mater. Res. Part B Appl. Biomater.* **2010**, *95B*, 84–90.

(36) Partlow, B. P.; Hanna, C. W.; Rnjak-Kovacina, J.; Moreau, J. E.; Applegate, M. B.; Burke, K. A.; Marelli, B.; Mitropoulos, A. N.; Omenetto, F. G.; Kaplan, D. L. Highly Tunable Elastomeric Silk Biomaterials. *Adv. Funct. Mater.* **2014**, *24*, 4615–4624.

(37) Ashby, M. F.; Gibson, L. J.; Wegst, U.; Olive, R. The Mechanical Properties of Natural Materials. I. Material Property Charts. *Proc. R. Soc. A Math. Phys. Eng. Sci.* **1995**, *450*, 123–140.

(38) Knowles, T. P. J.; Buehler, M. J. Nanomechanics of Functional and Pathological Amyloid Materials. *Nat. Nanotechnol.* **2011**, *6*, 469–479.

Acknowledgements

This work is supported by the Welcome Trust, ERC, Alzheimer Association Zenith, ALS Canada-Brain Canada, Canadian Institutes of Health Research and the Cambridge Centre for Misfolding Diseases. The authors would like to thank S. Zhang, Y. Lu and K. L. Saar for their help in fabrication of the microfluidic devices. K.H. Muller for the help of flash freezing and SEM imaging. And A. Alexiadis for the discussion in fluidic mechanics calculation.

Authors Contributions

Y.S. and T.P.J.K. conceived and designed the study. Y.S., S.F.R., A.K. and A.L. performed the experiments. Y.S., S.Q., P.StGH., C.I., S.A. and A.K. produced the materials. S.F.R. performed AMF-IR and analyzed the data. D.V. simulated the flow field. Y.S. imaged the samples under SEM, fluorescent microscope, ran microfluidic experiments and FRAP analysis. A.K. performed tensile strength measurement. Y.S., S.F.R., D.V., A.K. P.StGH, S.A. and T.P.J.K. analysed the data. All the authors contributed to the writing of the manuscript.

Competing financial interests

The authors declare no competing financial interests.

Methods

Proteins/Peptide sample preparation

FUS: cDNA encoding FUS (amino acid residues 1-526) was cloned into a baculovirus expression system vector, pACEBac2, with a protease cleavable N-terminal MBP tag and a C-terminal GFP-6xHis or mCherry-6xHis tag. The protein phase separate in the same manner without cleaving the tags[5–7]. The purified recombinant bacmid encoding FUS was transfected into Sf9 insect cells. The protein was expressed for 4 days post infection with the baculovirus harbouring the recombinant bacmid. The cell culture was harvested by centrifugation at 4,000 rpm for 30 min. The cell pellet was homogenised into the lysis buffer containing 50 mM Tris, 1 M KCl, 0.1% CHAPS, 1 mM DTT, 5% glycerol at pH 7.4. Post lysis the sample containing the protein was spun at 40,000 rpm in an ultracentrifuge to remove the cell debris. The supernatant was collected and processed using three steps purification protocol including, Ni-NTA affinity column, amylose affinity column and the final polishing step of size exclusion chromatography in the buffer containing 50 mM Tris, 1 M KCl, 1 mM DTT, 5% glycerol, pH 7.4. The final purity of the protein was greater than 95%. LLPS was induced by diluting the FUS solution in the 50 mM Tris buffer at final concentration 2 µM (FUS) and 50 mM (KCl) respectively.

Annexin A11: cDNA encoding the full length Annexin A11(amino acid residues 1-505) was cloned into pACEBac2 vector with a TEV cleavable N-terminal MBP tag and a C-terminal Cherry-His tag. The protein was expressed and purified from insect Sf9 cells. After 6 days of infection, cells were harvested and lysed by homogenising into a resuspension buffer containing 50 mM HEPES, 100 mM NaCl, 1 mM EDTA, 5% glycerol, 0.1% CHAPS, pH 7.4. Protein purification was undertaken as described above for FUS protein, using a three-step purification scheme. The final buffer used for Annexin A11 was 50 mM HEPES, 225 mM NaCl, pH 7.4. The final purity of the protein was greater than 95%. An Annexin A11 solution at concentration of 10 µM was mixed with dextran to induce the LLPS.

DED1: cDNA encoding Ded1 was cloned into a baculovirus expression system vector, pOCC120, with a GST protease cleavable N-terminal MBP tag and a C-terminal GFP and GST protease cleavable 6xHis tag. SF9 insect cells were transfected with recombinant baculovirus stocks and incubated for four days. The cells were harvested by centrifugation (15 min 500 x g), resuspended in 30 mL of lysis buffer (50 mM Tris/HCl, pH 7.6, 1 M KCl, 1 mM DTT, 1 protease inhibitor tablet with EDTA/50 ml buffer, 2 mM EDTA, 10 µl benzonase (250U/mL) and lysed using the EmulsiFlex-C5 (Avestin, Ottawa, Canada). The lysates were clarified by centrifugation (16,000 rpm for 1 h at 4°C, rotor JA 25.50, Beckman Coulter, Brea, California, USA). The supernatant was incubated with amylose resin for 1 h at 4°C and loaded onto a 20 ml chromatography column (Bio-Rad, Hercules, CA, USA). After washing 3 column volumes with wash buffer (50 mM Tris, pH 7.6, 1 M KCl, 1 mM DTT, 2 mM EDTA), the protein was eluted with elution buffer (wash buffer plus 20 mM maltose). Dialysis of the protein as well as cleavage of the tags (His and MBP) was performed overnight at 4°C in wash buffer with 0.01 mg/ml GST-3C Protease. The protein aggregates were removed by centrifugation in Falcon Tubes for 4 min at 3452 x g. The protein was concentrated using Amicon Ultra-15-30k centrifugal filters at 3452 x g. The proteins were loaded onto an Äkta Pure chromatography setup (GE Healthcare, Uppsala, Sweden) equipped with a Superdex 200 26/60 column or Superdex 200 16/60 column (GE Healthcare, Piscataway, NJ, United States). After SEC, the protein was concentrated by centrifugation using Amicon Ultra 15-30k centrifugal filters (Merck, Kenilworth, NJ, USA) at 3452 x g. The protein was flash-frozen using liquid-nitrogen and stored at -80°C.

zFF: Carboxybenzyl (Z)-protected diphenylalanine (zFF) dipeptide was purchased from Bachem (Switzerland). Z-FF was dissolved to a concentration of 100 mg/ml in DMSO and was then diluted further into a 10 % dextran solution to induce the LLPS.

PR25: The peptide with 25 repeats of proline-arginine (PR25) was purchased from GenScript (Hong Kong). PR25 was dissolved in water and then mixed with polyU at final concentration 100 μM and 1 μg/μl respectively to induce the LLPS.

Reconstituted Silk Fibroin (RSF) preparation: Silk protein was prepared based on a well-developed protocol[39]. Bombyx mori silk cocoons (Mindsets (UK) Limited) were cut into pieces and placed in a beaker containing a solution of 0.02 M sodium carbonate. The solution was boiled for 30 minutes and then the insoluble fibroin was removed from beaker. The fibroin was rinsed with water for three times and left for 3 days at room temperature to dry out. A 9.3 M lithium bromide solution was added to the dried silk fibroin in a 1:4 ratio of silk fibroin to lithium bromide. The mixture was heated at 65 °C for 4 h. The resulted solution was then dialysed against Mili-Q water in order to remove LiBr. The solution was left for 48 h at 4 C° while changing the water for 6 times in total. The dialyzed solution was then centrifuged at 9,000 rpm at 4 C° for 20 min to remove the remaining impurities. The centrifuge process was repeated twice, and the final solution was stored at 4 C°. A silk solution at concentration of 110 μg/ml was mixed with dextran to induce the LLPS.

Thioflavin T (ThT) staining

The β-sheets formation in the droplets and fibres was monitored by ThT staining. A final concentration of 100 μM ThT was used. The fluorescence images were taken under a Zeiss Fluorescent microscope with mercury fluorescent lamp. The filter with excitation wavelength of 440 nm and an emission wavelength of 480 nm was used. Objective 20X was used for Fig. 1a and oil immersion 100X was used for Fig. 1b. In more details, we first lowered the salt concentration to induce the LLPS of FUS. We then measured the fluorescence signal in the same pictures when there were both droplets and fibres. We measured ≥10 droplets and 3 fibres with 10 different locations on one fibre per protein/peptide. For different proteins and peptide we used the same fluorescent imaging settings (including light intensity and exposure time), and we used directly the raw data of the fluorescence signal comparison in Fig 1c. The two-tailed T-test was applied for the statistical analysis.

Scanning Electron Microscopy (SEM)

FUS droplet samples within 10 min after LLPS were briefly dipped twice in de-ionised water to remove any buffer salts and quickly plunge-frozen by dipping into liquid nitrogen-cooled ethane. Then, samples were freeze-dried overnight in a liquid nitrogen-cooled turbo freeze-drier (Quorum K775X). After that, the samples were mounted on aluminium SEM stubs using conductive carbon sticky pads (Agar Scientific) and coated with 15 nm iridium using a Quorum K575X sputter coater. The images were taken by using a FEI Verios 460 scanning electron microscope run at 2 keV. Secondary electron images were acquired using a high resolution Through-Lens detector in full immersion mode. Fibres were pulled from the LLPS solution and directly air dried and coated with 10 nm platinum. MIRA 3 FEG-SEM (TESCAN) was used in the 2 kV SE mode to take the images.

Flow field simulation

Numerical simulations were performed using COMSOL Multiphysics 5.2a (Massachusetts, USA). To obtain the 3D flow field of the complete microfluidic device the one-phase laminar flow physics was used. We modelled the aqueous protein suspension as water (via the built-in material's library) and used no-slip boundary conditions at the walls. The flow rate at each inlet was set as a laminar inflow and the

outlets were set at zero pressure with suppressed backflow. The velocity and pressure were extracted from a surface parallel to the xy plane at z = 2 μm, correspondent to the middle plane of the narrow bridges. The mean shear rate was obtained by averaging the shear rate values extracted from the cross-section at the centre of a narrow bridge. The shear stress is then simply obtained from the shear stress by multiplying it by the dynamic viscosity.

FTIR

Attenuated total reflection infrared spectroscopy (ATR-FTIR) was performed using a Bruker Vertex 70 spectrometer equipped with a diamond ATR element. The resolution was 4 cm^{-1} and all spectra were processed using Origin Pro software. The spectra were averaged (3 spectra with 256 co-averages), smoothed applying a Savitzky-Golay filter (2^{nd} order, 9 points) and then the second derivative was calculated applying a Savitzky-Golay filter (2^{nd} order, 11 points).

Infrared Nanospectroscopy

A nanoIR2 platform (Anasys, USA), which combines high resolution and low noise AFM with a tunable quantum cascade laser (QCL) with top illumination configuration was used. The samples morphology was scanned by the nanoIR microscopy system, with a rate line within 0.1-0.4 Hz and in contact mode. A silicon gold coated PR-EX-nIR2 (Anasys, USA) cantilever with a nominal radius of 30 nm and an elastic constant of about 0.2 N m^{-1} was used. To study polarisation effects, the IR light was polarized parallel and perpendicular the surface of deposition[21]. Both spectra and images were acquired by using phase loop (PLL) tracking of contact resonance, the phase was set to zero to the desired off-resonant frequency on the left of the IR amplitude maximum, and tracked with an integral gain I=0.1 and proportional gain P=5[40]. All images were acquired with a resolution of at least 500x500 pixels per line. The AFM images were treated and analysed using SPIP software. The height images were first order flattened, while IR and stiffness related maps where only flattened by a zero-order algorithm (offset). Nanoscale localised spectra were collected by placing the AFM tip on the top of the FUS droplets or fibres with a laser wavelength sampling of 2 cm^{-1} with a spectral resolution of 4 cm^{-1} and 256 co-averages, within the range 1400-1800 cm^{-1} [41]. Within a droplet or a fibre, spectra where acquired at a least 3 different nanoscale localised positions, the spectrum at each position being the average of 5 spectra. The average spectrum of the different was subtracted by the baseline signal of the substrate and salt[42]. Successively, the spectra were smoothed by Savitzky-Golay filter (second order, 9 points) and normalized. Spectra second derivatives were calculated, smoothed by Savitzky-Golay filter (second order, 9 points). Relative secondary and quaternary organization was evaluated integrating the area of the different secondary structural contribution in the amide band I, as previously shown in literature[19,43,44]. The error in the determination of the relative secondary structure content is calculated over the average of at least 5 independent spectra and it is < 5%. Spectra were analysed using the microscope's built-in Analysis Studio (Anasys) and OriginPRO. All measurements were performed at room temperature and with laser power between 1-4% of the maximal one and under controlled Nitrogen atmosphere with residual real humidity below 5%.

Microfluidics

The microfluidic channels were fabricated based on previous protocols[45], using polydimethylsiloxane (PDMS) (Sylgard 184 kit, Dow Corning, Midland, MI, USA) with a positive mode made by SU-8 on a silicon wafer. The two-layer SU-8 master was made by exposing twice, one with a chrome mask and the other one with a film mask under UV. The channels were plasma-treated and prefilled with tris buffer. The samples were flown in with precisely controlled flowrate with a syringe pump (Cetoni

neMESYS, Cetoni GmbH, Korbussen, Germany). The bright field and fluorescence images were obtained from an inverted microscope (Axio Oberver A1, Zeiss, Cambridge, UK).

Fluorescence Recovery After Photobleaching (FRAP)

FRAP was performed on a confocal microscope (Leica TCS SP8, Leica Microsystems GmbH, Wetzlar, Germany) with a 60X oil immersion objective, by using spot bleaching mode with a spot size of 0.45 µm in diameter. 1 ms bleaching time with 11% of the power of a 488 nm laser Argon was used. The fluorescence recovery was recorded with 0.5% of the power of the 488 nm laser every second for 175-200 seconds. The fluorescence intensity in the bleached spot was detected over time after bleaching and normalized with the photobleaching of the whole image from the recording. For the samples that drifted during the recording, we performed a "NanoJ-Core, Drift Correction" using ImageJ software platform prior to the FRAP analysis. The FRAP was conducted on at least three independent samples to get the average values with ±SD as error bars in Fig. 3e. The solid lines were drawn to guide the eyes. In Fig. 3f, the recovery at 170s was extracted from Fig. 3e and the two-tailed T-test was applied for the statistical analysis.

Tensile strength analysis

Tensile testing was performed using Tinius Olsen 5 ST with 5 N load cell, with the crosshead speed of 1 mm/min. In order to calculate stress, the obtained force data was divided by the cross-section area of the fibre where the diameter was measured prior to the testing using optical microscopy. The stress data was smoothed taking moving average of 24 neighbouring elements (corresponding to 0.14 % of strain) in order to reduce noise.

Critical concentration measurement and Gibbs free energy calculation

Two identical samples of FUS droplets were first prepared at protein and salt concentration of 2 µM and 50 mM, respectively. Shear was then applied to one of the samples to form fibres by manually pulling the solution by a pair tweezers for 50 times. To be noted that in the fibre sample there might still be some droplets. The two samples were then washed twice, including the steps of centrifuging at 21130 rcf (relative centrifugal force) for 10 min at room temperature, removing the supernatant and redispersing the material left in 50 mM KCl tris buffer. After washing, the samples were recovered to the original volume with 50 mM KCl tris buffer and rest for 7 days. The concentration of the soluble protein monomer in the supernatant in both of the samples were measured by NanoDrop™2000 (Thermo Fisher Scientific, USA) at time points 1 h, 2 h, 4h, 6h and 7 days.

The Gibbs free energy was calculated through chemical thermodynamics *(1)* based on a previous study[46], where $C_c^{droplet}$ is the critical concentration of droplet sample at the equilibrium, k_B is the Boltzmann constant and T is the absolute temperature (in our case T = 298 K).

$$C_c^{droplet} = \exp\left(-\frac{\Delta G_{m,d}}{k_B T}\right) \qquad (1)$$

The free energy difference between monomeric and droplet states, $\Delta G_{m,d}$, was calculated to be -11.5 kJ/mol, whereas the free energy difference between monomeric and fibre state $\Delta G_{m,f}$ was -10.0 kJ/mol. The difference between droplet and fibre states was -1.5 kJ/mol.

Data availability

All the relevant data are included in the manuscript and supplementary information. More detailed protocols, calculation and analysis are available from the authors upon request.

References

(39) Rockwood, D. N.; Preda, R. C.; Yücel, T.; Wang, X.; Lovett, M. L.; Kaplan, D. L. Materials Fabrication from Bombyx Mori Silk Fibroin. *Nat. Protoc.* **2011**, *6*, 1612–1631.

(40) Ruggeri, F. S.; Šneideris, T.; Chia, S.; Vendruscolo, M.; Knowles, T. P. J. Characterizing Individual Protein Aggregates by Infrared Nanospectroscopy and Atomic Force Microscopy. *J. Vis. Exp.* **2019**, e60108.

(41) Müller, J.; Ballini, M.; Livi, P.; Chen, Y.; Radivojevic, M.; Shadmani, A.; Viswam, V.; Jones, I. L.; Fiscella, M.; Diggelmann, R.; *et al*. High-Resolution CMOS MEA Platform to Study Neurons at Subcellular, Cellular, and Network Levels. *Lab Chip* **2015**, *15*, 2767–2780.

(42) Ruggeri, F. S.; Vieweg, S.; Cendrowska, U.; Longo, G.; Chiki, A.; Lashuel, H. A.; Dietler, G. Nanoscale Studies Link Amyloid Maturity with Polyglutamine Diseases Onset. *Sci. Rep.* **2016**, *6*, 31155.

(43) Shimanovich, U.; Ruggeri, F. S.; De Genst, E.; Adamcik, J.; Barros, T. P.; Porter, D.; Müller, T.; Mezzenga, R.; Dobson, C. M.; Vollrath, F.; *et al*. Silk Micrococoons for Protein Stabilisation and Molecular Encapsulation. *Nat. Commun.* **2017**, *8*, 1–9.

(44) Yang, H.; Wang, K. Genomic Variant Annotation and Prioritization with ANNOVAR and WANNOVAR. *Nat. Protoc.* **2015**, *10*, 1556–1566.

(45) Xia, Y.; Whitesides, G. M. SOFT LITHOGRAPHY. **1998**.

(46) Levin, A.; Mason, T. O.; Adler-Abramovich, L.; Buell, A. K.; Meisl, G.; Galvagnion, C.; Bram, Y.; Stratford, S. A.; Dobson, C. M.; Knowles, T. P. J.; *et al*. Ostwald's Rule of Stages Governs Structural Transitions and Morphology of Dipeptide Supramolecular Polymers. *Nat. Commun.* **2014**, *5*, 5219.